PERGAMON

International Journal of Heat and Mass Transfer 43 (2000) 3907–3915

International Journal of HEAT and MASS TRANSFER

www.elsevier.com/locate/ijhmt

High Schmidt mass transfer in a laminar impinging slot jet flow

Mingyong Chen[a], Radek Chalupa[b], Alan C. West[b], Vijay Modi[a,*]

[a]*Department of Mechanical Engineering, Columbia University, New York, NY 10027, USA*
[b]*Department of Chemical Engineering, Columbia University, New York, NY 10027, USA*

Received 17 November 1999; received in revised form 4 February 2000

Abstract

In this paper, high Schmidt-number mass transfer to a line electrode in laminar impinging slot-jet flows is investigated experimentally and numerically. Slot-based Reynolds numbers from 220 to 690 are considered. The mass-transfer measurements, made by the electrochemical method on 100 μm electrodes, are compared to the computed wall shear via an established analytical relationship. The local shear is obtained from steady, two-dimensional flow-field simulations of the Navier–Stokes equations. The use of an isolated line electrode and a small electrode size (100 μm) makes it possible to resolve the sharp variations in shear and mass transfer in the stagnation region. Both the experimental and theoretical results show that the peak values in Nusselt number occur at a point one-half to one jet width away from the stagnation point. Earlier experimental studies of heat transfer (Prandtl number of 0.72) reported by Gardon and Akfirat [R. Gardon, J.C. Akfirat, Heat transfer characterstics of impinging two-dimensional air jets, ASME Journal of heat Transfer 101 (1966) 101–108] (referred to in the figures as GA66) and mass transfer by Alkire and Ju [R., Alkire, J. Ju, High speed selective electroplating with impinging two-dimensional slot jet flow, J. Electrochemical Society 134 (2) (1987) 294–299] (referred to in the figures as AJ87) were not able to observe this behavior near the stagnation point.

Keywords: Laminar flow mass transfer; High Schmidt number; Impinging slot jet; Thin electrode

1. Introduction

Impinging jet flows are widely employed in industry to achieve rapid mass or heat transfer rates. The advantage of an impinging-jet flow is a high, localized mass (or heat) transfer rate due to the thin hydrodynamic and concentration (or thermal) boundary layers within the stagnation region. The thickness of these boundary layers may be on the order of tens of microns [3]. Although turbulent flow is of interest in most industrial applications, laminar jet flow is desired for some applications in which high stagnation pressure should be avoided.

Some researchers [4,5] have simulated laminar jet flow using numerical methods. Law and Masliyah [4] reported that if a parabolic velocity profile is imposed at the slot jet exit, weak secondary recirculation on the impingement plate could occur. Using a perturbation method, Chin and Tsang [6] examined the flow and the mass transfer to a circular disk electrode located within the stagnation region of a laminar/turbulent impinging

* Corresponding author. Tel.: +1-212-854-2956; fax: +1-212-854-3304.
E-mail address: modi@columbia.edu (V. Modi).

0017-9310/00/$ - see front matter
PII: S0017-9310(00)00052-1

Nomenclature

B	width of the jet (m)
c	concentration of ferricyanide ion (mol m^{-3})
c_∞	bulk concentration of ferricyanide ion (mol m^{-3})
C_f	friction coefficient
D	diffusion coefficient of ferricyanide ions (m^2 s^{-1})
f	factor appearing in Eq. (10) ($f = \gamma_M L \cdot 2^{-1}\beta_M^{-1}$)
F	Faraday's constant ($F = 96{,}500$ C mol^{-1} eq^{-1})
H	jet-to-plate distance (m)
i_L	limiting current density (A m^{-2})
L	streamwise length of the line sensor (m)
Nu_x	local Nusselt number
Nu	average Nusselt number
p	pressure (N m^{-2})
Re	Reynolds number ($Re = v_{in} B \nu^{-1}$)
s	value of x coordinate at either leading edge or midpoint of sensor (m)
Sc	Schmidt number ($Sc = \nu D^{-1}$)
u	velocity component in x direction (m s^{-1})
v	velocity component in y direction (m s^{-1})
W	dimension of the channel in z direction (m)
W_s	dimension of the sensor in z direction (m)
x	x coordinate (m)
y	y coordinate (m)
z	z direction (m)

Greek symbols

α	$[\frac{(1+f)^{3/2}-(1-f)^{3/2}}{f}]^{2/3}$
β	τ_w/μ (s^{-1})
$\Gamma(4/3)$	the gamma function of 4/3 ($\Gamma(4/3) = 0.89298$)
γ	$d\beta/dx$ (m^{-1} s^{-1})
η	similarity transform variable (m)
μ	dynamic viscocity (kg m^{-1} s^{-1})
ν	kinematic viscocity (m^2 s^{-1})
ρ	density (kg m^{-3})
τ_w	shear stress on the wall (kg m^{-1} s^{-2})
φ	value of β at either leading edge or midpoint of sensor (s^{-1})

Subscripts

c	continuously active
in	nozzle exit
L	mass transfer rate limited
M	midpoint of the sensor
w	impingement wall
x	local

jet. Polat et al. [7] reviewed the numerical simulations of fluid flow and heat transfer in impinging jet systems. Webb and Ma [3] presented a detailed review of single-phase, liquid jet impingement heat transfer experiments.

Flow systems most closely related to the case at hand have been investigated by two other groups. Chin and Agarwal [8] have examined the local mass transfer rates of a submerged, oblique impinging, slot jet. Their particular flow cell consisted of an impingement plate and an unconfined nozzle — i.e. the top plate shown in Figs. 1 and 2 was not present in their experiments. The impingement plate supported the working electrode, which consisted of a nickel sheet with drilled circular holes, each in turn containing insulated, flush mounted Nickel wires (each 2 mm in diameter). During their experiments, all of the wires and the nickel plate were active reduction areas for ferricyanide ion, however current measurements were taken from only one nickel wire at a time. This set up may be referred to as a "continuously active geometry". In their study, the jet angle varied from 15° to 90° relative to the impingement plate. They have used a Reynolds number range of 1000–8000 and allowed the location of the nozzle to vary in the range $1 \le H/B \le 8$ in the vertical direction and $-24 \le x/B \le 32$ in the horizontal direction. Alkire and Ju [2] studied a similar system, the major differences being in the configuration of the working electrode and the fact that confined jets were also examined. In that particular case, the working electrode consisted of rectangular, flush mounted

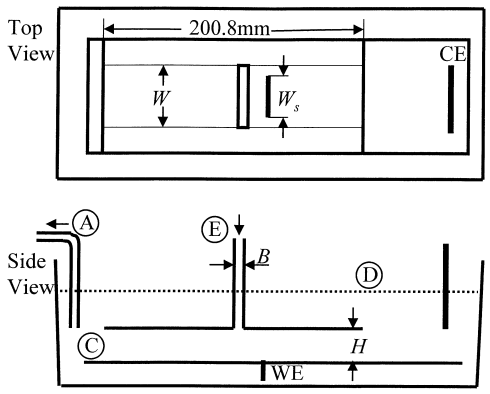

Fig. 1. Schematic diagram of the electrochemical cell and the solution holding tank. A, tubing to pump; C, impingement plate; D, solution level in the tank; E, tubing from pump; WE, working electrode; CE, counterelectrode.

nickel sheets ranging in size (in the flow direction) from 1.59 mm directly under the nozzle to 12.7 mm away from the nozzle and separated from each other by thin pieces of insulating material (another example of a continuously active geometry). In those experiments, Reynolds number varied from 500 to 2750 and the nozzle location assumed values in the range $H/B = 5$ and 9.4 in the vertical direction and $0.5 \leq x/B \leq 19.5$ in the horizontal direction.

In the current work, the fluid emerges from a slot nozzle to impinge onto a stationary, submerged plate, as shown in Fig. 2. Since a plate parallel to the impingement plate is employed, the problem is that of a confined, submerged impingement. The flow can be divided into three spatial regimes: the impingement region, located under the nozzle (i.e. approximately $0 \leq x/B < 3$); the transition region, located immediately downstream (i.e. approximately $3 \leq x/B < 6$); and channel flow downstream. The assumed coordinate system is also plotted in Fig. 2. For mass transfer measurements, the impingement plate is insulated except for a thin, rectangular strip (i.e. the mass transfer sensor or the working electrode) on the plate. The concentration on this thin sensor is maintained at a constant value of zero in accordance with the limiting current condition. The concentration along the upstream section of the impingement plate is set constant to a normalized value of one. Because the sensor is very thin ($L = B/35$) and the Schmidt-number of the fluid is very high, it is not necessary to solve the convective mass transfer equation in the entire calculation domain. Instead, an analytical solution relating the mass transfer rate to wall shear stress can be obtained by applying the boundary-layer theory, as was demonstrated by Burmeister [9] and Newman [10]. The shear stress on the impingement plate was calculated by solving the two-dimensional Navier–Stokes equations using the cell-centered finite volume method. Three-dimensional effect on mass transfer was also considered briefly.

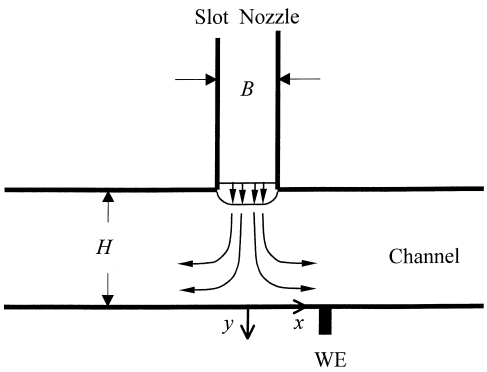

Fig. 2. Schematic diagram of the flow field within the impinging slot jet electrochemical cell and the assumed coordinate system. WE, working electrode; CE, counterelectrode.

2. Experimental

2.1. Flow cell design

The flow cell was made of transparent Plexiglass. Fig. 1 is a schematic of the flow cell positioned within the solution tank. The nozzle has inner cross-section $W \times B = 30.3$ mm $\times$ 3.5 mm and length 92.5 mm. Above the nozzle, the flow cell has a 126.7 mm long "neck" which gradually changes from its top cross-sectional dimensions of 24.5 mm $\times$ 22.5 mm to the dimensions of the nozzle at its bottom. The channel part of the flow cell is comprised of two vertical spacers and two plates, with the nozzle being attached to the top plate and the sensor being flush mounted in the bottom one. The two spacers are secured between the two plates by means of four Teflon bolts and nuts. The lengths of the top and bottom plates are 200.8 and 342.8 mm, respectively, thus allowing the bottom plate to be shifted relative to the top one (permitting the horizontal position of the sensor relative to the nozzle to be adjusted). The dimensions of the cross-section of this channel are $H \times 30.3$mm, where H can be adjusted by changing the pair of vertical spacers. Three sets of these spacers were used, allowing H to assume values of 3.2, 6.9, and 14.2 mm.

The mass transfer sensor consisted of 0.1 mm $\times$ 20.3 mm ($= L \times W_s$) platinum foil, casted in a cylindrical mold. The mold was mounted flush to the center of the bottom plate so that the working electrode (WE) is perpendicular to the flow direction. The counterelectrode (CE) is a 50 mm $\times$ 300 mm piece of nickel foil and was downstream of the working electrode mounted on the wall of the container near the outlet of the flow cell. The counterelectrode protruded above the liquid level in the tank allowing a simple electrical connection via an alligator clip.

The pump used in these experiments was a variable speed peristaltic unit (Masterflex L/S model 77250-62). The uptake end of the tubing was submerged in the tank away from the flow cell, while the feed end of the tubing is connected directly to the neck of the flow cell via a barbed connector. Flow rates ranging from 6.0 to 22 cm^3/s were used.

2.2. Solution chemistry and measurement procedure

Experiments used 24 liters of electrolyte composed of 0.003 M potassium ferricyanide, 0.003 M potassium ferrocyanide, and 0.1 M potassium chloride. Reduction of ferricyanide ion takes place at the sensor and the reverse reaction takes place at the anode. The system's

temperature was 23 ± 2°C. The diffusivity of the ferricyanide ion, $D = 0.8 \times 10^{-5}$ cm^2/s, was taken from Yang et al. [11].

The flow rate was determined from the time required to drain 200 ml of solution from a graduated cylinder into the flow cell contained in the tank and fully submerged as during the experiments. Effects of the imposed pressure drops on the flow rate were studied by repeating the calibration with different vertical spacers in place.

Prior to pumping the electrolyte into the system, both tank and flow cell were thoroughly rinsed with deionized water several times and allowed to air dry. The solution was then poured into the tank. Care was taken before each trial to eliminate air bubbles from the flow system. Measurements were taken after about 30 s of a constant volumetric flow rate. A Pine Instruments AFRDE4 potentiostat was used to control potential and measure current (i.e. the mass transfer limiting current density, i_L). The potential was set at the limiting-current plateau, specifically at an overpotential of -700 mV vs. the counterelectrode. In addition, two Hewlett Packard 34401A multimeters were used, one for displaying the potential setting and the other for displaying the current and interfacing with the data acquisition software (Hewlett Packard 34812A BenchLink/Meter, version 1.0). A flow instability induced by the action of the peristaltic pump would occur within the frequency range of 0.5–2 Hz for the range of flow rates used. No apparent disturbances of matching frequencies were observed during data acquisition.

It was estimated that each adjustment of the sensor in the horizontal direction carried an uncertainty of ± 0.5 mm. For clarity this is shown only in the inset graphs of Figs. 7–9 by means of horizontal error bars, even though this uncertainty applies to all of the x/B settings. Experiments were repeated at least twice (each time with a fresh solution) to check for reproducibility. Experimental data presented in Figs. 7–9 represent algebraic means of the collected data, while the vertical error bars show the discrepancy between two data sets.

3. Fluid flow

In this paper, fluid dynamics simulations were carried out assuming a two-dimensional flow. This assumption is at its weakest in the case of the lowest channel aspect ratio used. As the fluid leaves the stagnation region, growth of boundary layers on the walls eventually leads to a fully- developed rectangular channel flow. For the largest H/B value, the channel aspect ratio, $W/H = 2.1$. Moreover, the cross-stream sensor dimension, W_s, is comparable to the channel width, W. Both these factors could potentially make the problem three-dimensional. For a fully-developed, rectangular channel flow the mass transfer rate on the sensor can be obtained using an expression for velocity profile given by Natarajan and Lakshmanan [12]. For the parameters of the present experiments, the departure from two-dimensionality is always found to be less than about 7%. This estimate is obtained only for fully-developed flow but can be expected to be lower in the impingement ($0 \le x/B < 3$) and the transition regions ($3 \le x/B < 6$).

The fluid flow is assumed to be a steady, incompressible, constant-property, two-dimensional, laminar flow. Viscous dissipation as well as buoyancy effects due to altered concentrations were neglected. With these assumptions the flow is mathematically described by the following equations:

$$\text{continuity,} \quad \frac{\partial u}{\partial x} + \frac{\partial v}{\partial y} = 0 \tag{1}$$

u momentum,

$$u\frac{\partial u}{\partial x} + v\frac{\partial u}{\partial y} = -\frac{1}{\rho}\frac{\partial p}{\partial x} + \nu\left(\frac{\partial^2 u}{\partial x^2} + \frac{\partial^2 u}{\partial y^2}\right) \tag{2}$$

v momentum,

$$u\frac{\partial v}{\partial x} + v\frac{\partial v}{\partial y} = -\frac{1}{\rho}\frac{\partial p}{\partial y} + \nu\left(\frac{\partial^2 v}{\partial x^2} + \frac{\partial^2 v}{\partial y^2}\right) \tag{3}$$

The boundary conditions were specified as follows. At the jet exit, a fully-developed laminar flow is assumed. At the impingement and confinement walls, no slip velocity conditions are imposed. At the symmetry boundary, standard symmetry conditions are imposed on both the velocity and the pressure. At the outlet boundary, the first derivative of the velocity components along the streamwise direction is assumed to vanish and the pressure is specified to be atmospheric. The second derivative of pressure is assumed to vanish at the jet exit as well as on the walls. A cell-centered finite volume approach based on the artificial compressibility method is employed to solve the velocity field. Details of the computational approach are given in [13]. After obtaining the flow field, the friction coefficient on the impingement plate is calculated from:

$$C_f = \frac{\mu\beta}{\frac{1}{2}\rho v_{in}^2} \tag{4}$$

where $\beta = \tau_w/\mu$.

4. Mass transfer

In the present paper, the active mass transfer region was a very thin strip on the impingement plate ($L/B = 0.03$) assumed to be centered at $x = x_M$. Thus, in order to avoid resolution problems near the thin strip, boundary layer theory was applied to solve the two-dimensional convective diffusion equation. With the assumption that forced convection dominates over diffusion in the flow direction (the x direction), the equation is simplified to:

$$u\frac{\partial c}{\partial x} + v\frac{\partial c}{\partial y} = D\frac{\partial^2 c}{\partial y^2} \tag{5}$$

The two velocity components in the above equation, u and v, are assumed to have the forms:

$$u = y\beta(x) \text{ and } \quad v = -\frac{1}{2}y^2\gamma(x) \tag{6}$$

where $\beta(x) = \frac{\partial u}{\partial y}|_{y=0}$ and $\gamma(x) = \frac{d\beta}{dx}$. The boundary conditions for the above convective diffusion equation are: $c = c_\infty$ at $x = x_M - L/2$, $c = 0$ at $y = 0$ and $x_M - L/2 < x < x_M + L/2$, and $c = c_\infty$ as y approaches infinity. Solution to the above problem is described in [10]. From that result and the definition of local Nusselt number,

$$Nu_x = \left(\frac{B}{c_\infty}\right)\frac{\partial c(x,y)}{\partial y}\bigg|_{y=0} \tag{7}$$

one can obtain the expression for local Nusselt number in terms of $\beta(x)$

$$Nu_x = \frac{B}{9^{1/3}\Gamma(4/3)}Sc^{1/3}\sqrt{\beta(x)}\left[\nu\int_s^x \sqrt{\beta(\eta)}\,d\eta\right]^{-1/3} \tag{8}$$

where $s = x_M - L/2$ away from the stagnation point, and $s = x_M$ for the case of sensor being centered directly under the nozzle. Since the sensor is very thin, the wall shear stress can be assumed to vary linearly along the sensor width, L. With this assumption, one obtains the following equation:

$$Nu_x = \frac{B}{6^{1/3}\Gamma(4/3)}Sc^{1/3}\left(\frac{\gamma_M}{\nu}\right)^{1/3}\frac{\sqrt{\beta_M + \gamma_M\Delta x}}{\left[(\beta_M + \gamma_M\Delta x)^{3/2} - \varphi^{3/2}\right]^{1/3}}$$

$$(x_M - L/2 < x < x_M + L/2) \tag{9}$$

where, $\phi = \beta_M - \gamma_M L/2$ away from the stagnation point and $\varphi = \beta_M$ at the stagnation point. Furthermore, $\Delta x = x - x_M$, and β_M and γ_M are the values of β and γ at the midpoint of the sensor, respectively.

For the case of the sensor being located away from the stagnation point, integration of Eq. (9) over the sensor width, L, gives the average Nusselt number (see also [14]):

$$Nu = \frac{1}{L}\int_{x_M - L/2}^{x_M + L/2} Nu_x\,dx$$

$$= \frac{1}{6^{1/3}\Gamma(4/3)}Sc^{1/3}\frac{B}{L}\left(\frac{\beta_M L^2}{4\nu}\right)^{1/3}\left[\frac{(1+f)^{3/2} - (1-f)^{3/2}}{f}\right]^{2/3} \tag{10}$$

where $f = \gamma_M L/2\beta_M$.

Numerically, Nusselt number (away from stagnation point) was obtained from fluid dynamics computations, specifically the friction coefficient, C_f (evaluated at the sensor's midpoint, i.e. x_M), via the relationship:

$$Nu = 1.01\alpha Sc^{1/3}C_f^{1/3}Re^{2/3} \tag{11}$$

The quantity α in the above equation is the factor within the square brackets in Eq. (10) containing the variable f. For a pure shear flow $f = 0$ and $\alpha = 3^{2/3}$.

At the stagnation point, the integration in Eq. (10) is carried out over half of the sensor width (i.e. in this case, lower limit of integration is x_M) and β_M goes to zero. Hence,

$$Nu = \frac{B}{6^{1/3}\Gamma(4/3)}Sc^{1/3}\left(\frac{\gamma_M}{\nu}\right)^{1/3} \tag{12}$$

Experimental mass transfer data can be compared with the results from Eqs. (11) and (12) by converting the

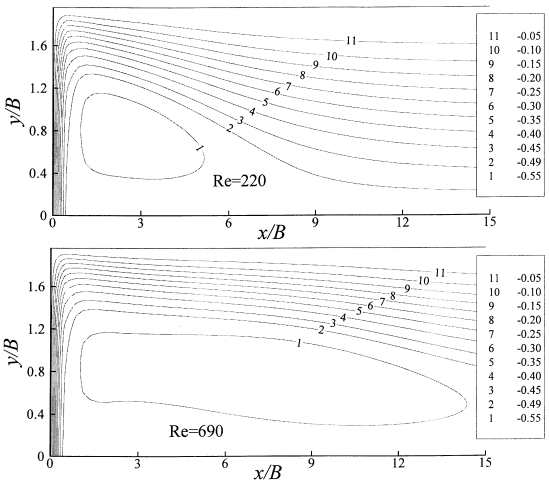

Fig. 3. Comparision of streamlines at two different Reynolds numbers for $H/B = 2.0$. Since the symmetric half of the flow is computed, the stream function at the confinement wall is -0.50. The stream function at the symmetry boundary, $x/B = 0$, and at the impingement plate, $y/B = 2.0$, has been set to 0.0.

limiting current density values, i_L, into Nusselt numbers (using Faraday's law) through:

$$Nu = \frac{Bi_L}{DFc_\infty} \tag{13}$$

5. Results and discussion

5.1. Mesh independence and code validation

Several tests were carried out to ascertain uncertainties in the numerical results as well to validate the results against existing analytical and experimental data. One source of uncertainty in the computed mass transfer results stems from the inability to accurately ascertain the friction coefficient C_f along the impingement wall under conditions of incipient separation [4]. In order to illustrate this, typical streamlines for two different flow simulations at $Re = 220$ and 690 for $H/B = 2.0$ are shown in Fig. 3 for a grid of 80×80. For a stringent Re of 690, further grid refinement leads to a small recirculation region in the x/B range of 12–20. While the numerics are unable to capture this recirculation region accurately, their effect on C_f was estimated to be about ± 0.002 at $x/B = 15$. Since this uncertainty occurs in a region of low shear, the corresponding uncertainty in the mass transfer can be much higher. This is shown in Fig. 4 by means of a plot of Nusselt number for four different grids. The corresponding experimental data are also shown in Fig. 4. The region of the largest disagreement between the computational results and the experimental data is in the x/B range of 3–10. In this region, however, the simulations do not show any significant uncertainties. Consequently, all subsequent simulations are shown with a grid of 80×80.

The first code validation test was carried out by computing the friction coefficient on the impingement wall in the fully-developed flow region. In this region the problem reduces to that of a fully developed channel flow for which an exact solution is available. The test was carried out for $H/B = 0.9$ and $Re = 220$. The results show good agreement as seen in Fig. 5. The maximum relative error of all the numerical friction coefficients is less than 5%.

The second code validation test was carried out by computing heat transfer from a laminar, impinging slot jet. Here, computed heat transfer coefficients were compared with the experimental data of Gardon and Akfirat [1]. In their study, the entire impingement plate was heated (a set up which in this paper has been referred to as a continuously active geometry) and hence local data were acquired by segmenting the plate into sections of finite length, with the smallest section ($0.6B$ in size) being near the stagnation region. Note that heat transfer coefficients in [1] are normalized to obtain a local Nusselt number, Nu_c, and further normalized with $Pr^{1/3}$ for the purpose of comparison with numerical results. The simulations were carried out for $H/B = 4$, $Re = 450$, $Pr = 0.72$ (for air), and a calculation domain length of 80B. The numerical and experimental Nu_c values along the wall are shown in Fig. 6. The results exhibit a peak in the heat transfer coefficient at the stagnation point. Agreement between the

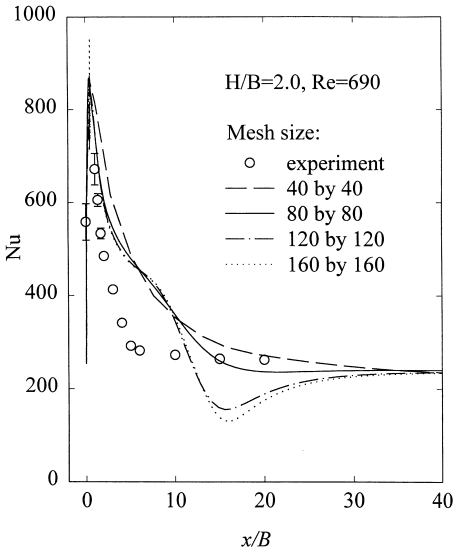

Fig. 4. Variation of Nu with x/B for three different mesh sizes.

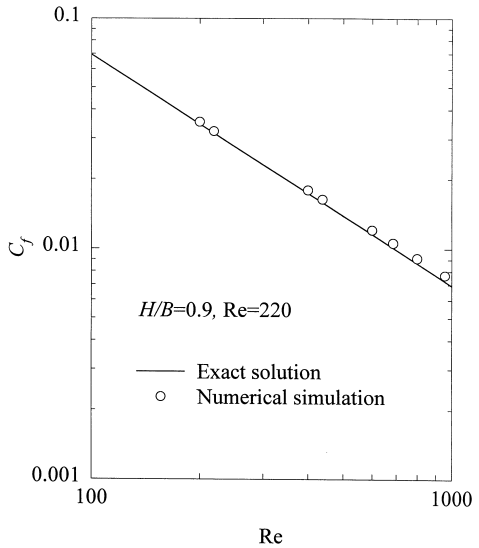

Fig. 5. Comparision of numerical results of fully-developed friction coefficient C_f with the exact solution.

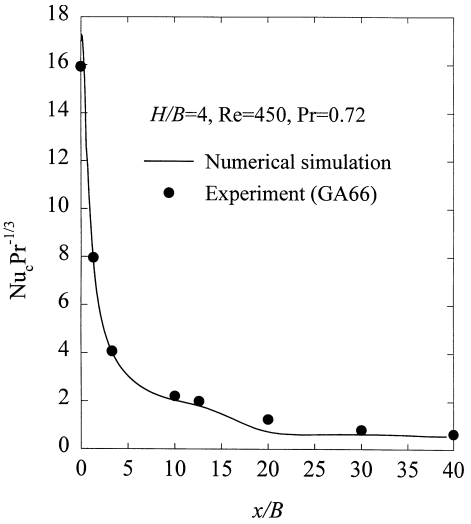

Fig. 6. Comparision of numerical results of heat transfer coefficient Nu_c with Gardon and Akfirat's [1] experimental data.

numerical simulations and experimental data is very good in the entire domain.

5.2. Computed and experimental results

Experimental data, showing the variation of mass transfer rate, *Nu*, with x/B were acquired for three different flow rates and for three different nozzle-to-plate (H/B) distances, as shown in Figs. 7–9. The length of the calculation domain in the x direction was chosen to ensure that further increases in length would not alter the calculation results in the original domain. Theoretical Nusselt number values in Figs. 7–9 were obtained from Eqs. (11) and (12). The variables β_M and γ_M appearing in those equations were computed using the flow solver.

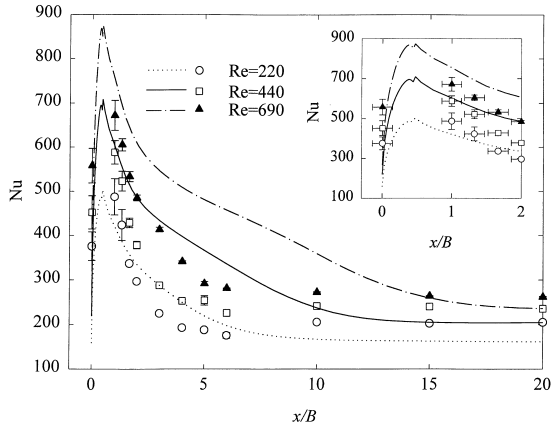

Fig. 8. Variation of *Nu* with x/B for $H/B = 2.0$ (lines: simulation; symbols: experiments).

Both the theoretical results and the experimental data show that the mass transfer is relatively low at the stagnation point. However, a sharp increase is observed as one moves away from the stagnation point reaching a maximum between x/B values of 0.5–1. Subsequently, the Nusselt number drops quickly and approaches a constant value corresponding to that in a fully-developed channel flow. Note that the behavior in the stagnation region is different from the results of Gardon and Akfirat [1], and Alkire and Ju [2] which were acquired with continuously active geometries. At the stagnation point, the theoretical results for mass transfer are much lower than the experimental data. This deviation could be due to the experimental uncertainty in positioning of the line sensor. Since the mass transfer coefficient increases very rapidly near the stagnation point, any small departure of the line sensor from the stagnation point will cause a sharp increase in Nusselt number. The results also show that the peak

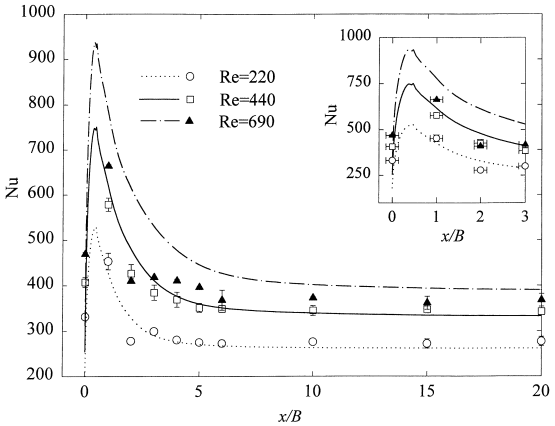

Fig. 7. Variation of *Nu* with x/B for $H/B = 0.9$ (lines: simulation; symbols: experiments).

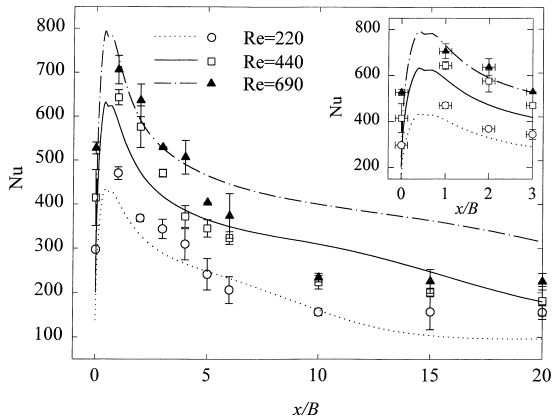

Fig. 9. Variation of *Nu* with x/B for $H/B = 4.1$ (lines: simulation; symbols: experiments).

values of computed and measured Nusselt numbers differ. This, however, can be attributed to the fact that the peak in mass transfer occurs at about $x/B = 0.5$ in the simulations, whereas the experimental data are obtained at $x/B = 0.0$ and 1.0 (see the insets of Figs. 7–9).

In the transition region (i.e. $3 \leq x/B < 6$), the agreement between the theory and experiment is generally reasonable at lower Reynolds numbers. On the other hand, for $Re = 690$ the agreement is particularly poor, with the experimental results being consistently lower than the predicted numerical values. This can probably be explained with the aid of the streamline plots in Fig. 3. For $Re = 690$, a large recirculation region near the confinement wall extends as far downstream as $x/B = 15$. At the higher Reynolds number of 690, the flow in this recirculation region may be particularly susceptible to flow unsteadiness during the experiments. This unsteadiness would cause enhanced mixing leading to a more rapid approach to fully developed channel flow [15]. The early approach to fully-developed values cannot be explained by three-dimensional effects on the hydrodynamic entrance length, since three-dimensionality has been shown to increase the entrance length [16,17].

5.3. Discussion

There are two different approaches to obtaining impingement wall mass transfer data or carrying out simulations. One approach is that adopted in the present study where a single small (100 μm or $L/B = 1/35$) isolated electrode is utilized and the rest of the impingement plate is rendered inactive. Experimentally this provides the advantage of being able to use a single sensor (embedded in the impingement plate) which can be moved relative to the jet in order to carry out measurements along the entire wall. All the experiments carried out in the present study were of this nature. From a computational standpoint, this scenario also makes it easier to compute mass transfer once the fluid flow is known since a theoretical formula for a thin electrode can be used.

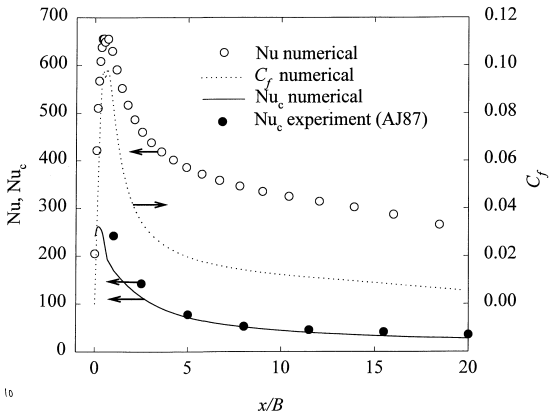

Fig. 10. Comparision of mass transfer coefficients on a thin electrode and a continuously active plate ($H/B = 5$, $Re = 500$, $Sc = 2400$).

The second approach is to maintain the entire impingement plate active. This approach, however, requires one to segment the plate into many small sections in order to measure the local mass transfer rate. From a computational standpoint, this scenario is more difficult to implement, since, in general, one has to now solve the concentration equations in the entire domain. Moreover, the grid for the mass transfer simulation must be significantly finer than that for the flow field simulation because of high Schmidt number. In order to highlight the differences in these scenarios, simulations were carried out using both of these approaches. The results are shown in Fig. 10 by means of open circles for the isolated line sensor and a solid line for the continuous electrode. The line sensor plot consists of mass transfer results averaged over the length of the electrode (in the flow direction), whereas the continuous electrode results are simply the local Nusselt number values. Both of these sets of computations were carried out at $Re = 500$, $H/B = 5$, and $Sc = 2400$. Note that these parameters are different from those in the previous figures in order to permit comparison with the experimental data of Alkire and Ju [2] for a continuous electrode.

In many advanced electronics applications, the impingement wall is neither a single isolated electrode nor a continuous electrode. Instead, it consists of a series of closely spaced but irregularly packed discrete electrodes separated by inactive regions. The important determinant of the ability to model this situation is the accuracy of fluid flow solution. As seen in Fig. 10, the line electrode approach adopted here is better able to discriminate between flow fields, since it is more adept at capturing the variations in local shear. A continuous electrode may mask some of the finer differences in flow, since its response is governed by both the local shear and the depletion in the electrolyte due to larger distances from the leading edge of the concentration boundary layer.

The results for the continuous electrode study of Alkire and Ju [2] are also shown in Fig. 10. Their results agree well with the continuous electrode simulations despite the fact that their experiments have two differences from the present study. The first difference, which is significant, is the location of the confinement wall. This confinement wall, in [2], is still parallel to the impingement wall but is not flush with the jet exit and is instead recessed by a distance of $32B$. Hence, their distance between the confinement wall and the impingement wall is $37B$. This geometry difference

would alter the local shear except perhaps in the impingement region. The other difference is that in the Alkire and Ju's [2] study, the electrode sizes are quite large and the smallest electrode is of size B. Moreover, their active region begins at $x/B = 0.5$ and not 0 as in the present study. Hence, their first electrode extends from $x/B = 0.5$ to 1.5, with the first data point shown in Fig. 10 being at $x/B = 1.0$. Since their measurement represents an average value over this electrode, the variation of Nusselt number near the stagnation point is masked. Simulations in the present work show that even for the continuous electrode case the peak in mass transfer rate does not occur at the stagnation point. Note that the definitions of Reynolds number and Nusselt number in [2] are different from those given in this paper and have been converted for the purpose of comparison.

6. Conclusions

Mass transfer to a flush-mounted, line electrode located on a plate with a submerged, confined, laminar slot jet impinging on it is examined. Both numerical and experimental investigations of this flow system clearly capture the fact that the peak in the mass transfer rate does not occur directly underneath the slot nozzle. This peak in the Nusselt number is instead displaced about one-half to one nozzle width away from the nozzle centerline. Additionally, numerical and experimental results are in reasonable agreement within the impingement region, i.e. approximately $0 \leq x/B < 3$. Greater discrepancy between the two sets is seen in the transition region (i.e. $3 \leq x/B < 6$). It is here that the experimental Nusselt numbers diminish to their fully-developed channel flow values more quickly (i.e. at lower x/B settings) than the corresponding numerical results.

Small streamwise electrode size ($L \ll B$) or a very fine segmentation of the active surface in a continuously active geometry system is essential if one is to observe the peak in the mass transfer rate away from the stagnation point. Furthermore, the thin electrode method of mass transfer rate measurement is more sensitive to the wall shear stress than the continuously active geometry method, making thin, isolated electrodes better experimental tools for the validation of fluid dynamics computations.

Acknowledgements

This work was supported by the National Science Foundation under award number CTS-97-06824.

References

[1] R. Gardon, J.C. Akfirat, Heat transfer characteristics of impinging two-dimensional air jets, ASME Journal of Heat Transfer 101 (1966) 101–108.

[2] R. Alkire, J. Ju, High speed selective electroplating with impinging two-dimensional slot jet flow, J. Electrochemical Society 134 (2) (1987) 294–299.

[3] B.W. Webb, C.-F. Ma, Single-phase liquid jet impingement heat transfer, in: J.P. Hartnett, T. Irvine, Y.I. Cho, G.A. Green (Eds.), Advances in Heat Transfer, vol. 26, Academic Press, New York, 1995, pp. 105–217.

[4] H.S. Law, J.H. Masliyah, Mass transfer due to a confined laminar impinging two-dimensional jet, Int. J. Heat Mass Transfer 27 (4) (1984) 529–539.

[5] M.D. Deshpande, R.N. Vaishnav, Submerged laminar jet impingement on a plane, J. Fluid Mechanics 114 (1982) 213–236.

[6] D-T. Chin, C-H. Tsang, Mass transfer to an impinging jet electrode, J. of Electrochem. Soc. 125 (9) (1978) 1461–1470.

[7] S. Polat, B. Huang, A.S. Mujumdar, W.J.M. Dougas, Numerical flow and heat transfer under impinging jets: a review, in: C.L. Tien, T.C. Chawla (Eds.), Annual Reviews of Numerical Fluid Mechanics and Heat Transfer, vol. 1, Hemisphere, New York, 1989, pp. 157–197.

[8] D-T. Chin, M. Agarwal, Mass transfer from an oblique impinging slot jet, J. Electrochem. Soc. 138 (9) (1991) 2643–2650.

[9] L.C. Burmeister, in: Convective Heat Transfer, Wiley, New York, 1983, pp. 349–350.

[10] J.S. Newman, in: Electrochemical Systems, 2nd ed., Prentice Hall, Englewood Cliffs, 1991, pp. 356–359.

[11] D. Yang, A. Shehata, V. Modi, A. West, Mass transfer to a channel wall downstream of a cylinder, Int. J. of Heat and Mass Transfer 40 (18) (1997) 4263–4271.

[12] N.M. Natarajan, Lakshmanan Laminar flow in rectangular ducts: prediction of velocity profiles & friction factor, Indian Journal of Technology 10 (1972) 435–438.

[13] H. Cabuk, C.-H. Sung, V. Modi, Explicit Runge–Kutta method for three-dimensional internal incompressible flows, AIAA Journal 30 (8) (1992) 2024–2031.

[14] R.J. Goldstein, Fluid Mechanics Measurements, Hemisphere, New York, 1983, pp. 572–577.

[15] W.S. Janna, Introduction to Fluid Mechanics, 2nd ed., PWS, Boston, 1987, pp. 175–176.

[16] C.L. Winginton, C. Dalton, Incompressible laminar flow in the entrance region of a rectangular duct, J. Applied Mechanics 37 (1970) 854–856.

[17] L.S. Han, Hydrodynamic entrance lengths for incompressible laminar flow in rectangular ducts, J. Applied Mechanics 27 (1960) 403–409.